RESEARCH ARTICLE-CHEMISTRY

Synthesis and Study of Zinc Oxide Nanorods as an Adsorbent Material for the Removal of Carcinogenic Dye and Anticancer Activities

V. N. Kowshalya[1] · **P. N. Palanisamy[1]**

Abstract

The present research work targets the synthesis of cost effective nano-zinc oxide and study on efficiency of the synthesized materials towards treatment of hazardous carcinogenic dye from wastewater by adsorption process. In addition to treatment of wastewater, biomedical application of the synthesized zinc oxide nanorods is also tested for its aniticancerous activity. Prepared nano-zinc oxide is characterized by XRD, SEM, EDX, BET, UV-DRS and Raman spectroscopy. The BET analysis data confirmed the larger pore size and hence the easy diffusion of dye molecules into the sorbent material. From the analysis of experimental data the pseudo-first-order model with r^2 value of 0.9988 showed better fit than the pseudo-second-order model. Adsorption of AO7 on ZnO nanostructures evidenced by n value of Frendluich isotherm authenticating the multilayer adsorption on heterogeneous surface of the sorbent material. Furthermore, thermodynamic parameters proved the spontaneous, exothermic nature of the adsorption process. The AO7 removal efficiency of 97% under optimal conditions of adsorbent dose of 100 mg, temperature of 30 °C, initial dye concentration of 50 mg/L and initial pH of 8.0 are observed. The cytotoxic effect of the synthesized zinc oxide nanorods was also evaluated using MTT assay. The significant cytotoxic efficacy (IC50) induced by the synthesized zinc oxide nanorods against human melanoma cancer is found to be 11.3 μg/ml.

Keywords Zinc oxide nanorods · Adsorption · Nanomaterial · Nonlinear curve fitting · Anticancer activity

1 Introduction

Textile dye wastewater is one of the highly addressed problems of the world environmental concerns. Most of the industries use different dyes to colour their fabrics. Effluents are highly coloured and degradation of the dyes in water bodies releases secondary pollutants into the environment. It may also affect photosynthetic activities of aquatic vegetation by reducing the diffusion of sun light. Among the different types of dyes, azo dye, benzidine dyes, etc., are non-biodegradable and/or undergo some partial degradation to form harmful by-products which are carcinogenic in nature [1]. Most of the industries withdrawn the uses of benzidine and benzidine based dyes for colouring their fabrics [2], but still it is used in some of the processing industries. One among such renowned dye, Acid Orange 7 (AO7), is widely used in

textile, paper, food industries, etc. When effluent containing the dye is released into the environment, causes severe adverse effects such as damages to skin, eyes, digestive system, respiratory irritation, aesthetic issues, mutagenic and carcinogenic effects. So the researchers takes more attention towards the treatment of such potential pollutants by different treatment processes like electrocoagulation, adsorption, photocatalyst, membrane treatment, advanced oxidation process, etc., to make the sustainable environment [3, 4]. Table 1 explores the details of percentage of degradation of AO7 dye by various methods.

Cancer has high morbidity and mortality worldwide. Melanoma is an aggressive type of skin cancer and its characteristics include multi drug resistance, high relapse rate and low survival rate. Nowadays, apart from traditional chemotherapy and surgery in the treatment of cancer, nanoparticles are also used due to their selective targeting capability [10]. Among various nanomaterials, zinc oxide nanostructure has gained importance due to its opto-electrical, antimicrobial, anti-proliferative, catalytic and photochemical properties [11]. Zinc Oxide (ZnO) is the second most abundant metal oxide and is considered a "Generally

✉ V. N. Kowshalya
  kowshinila@gmail.com

[1] Centre for Environmental Research, Department of Chemistry, Kongu Engineering College, Perundurai, Erode, TamilNadu 638060, India

Table 1 Percentage of degradation of AO7 by various methods

Method of degradation	Material used	Percentage of degradation (%)	Reference
Adsorption	Kenya Tea residue	98.41	[5]
Adsorption	Aluminium oxide Nanoparticles	100	[6]
Adsorption	Polypyrrole/nanosilica composite	99.4	[7]
UV	Acetylacetone	99	[8]
Electrochemical degradation	Boron doped diamond electrode	98	[9]

Recognised As Safe (GRAS)" compound by US Food and Drug Administration. It is vital for various cellular mechanisms and also helps in maintaining cellular homeostasis, hence its biocompatibility.

Among the different materials used for environmental concern, ZnO is a semiconductor with a wide direct-band gap of 3.3 eV. ZnO and ZnO-related materials have attracted more and more attention over the past decades because of its applications in various fields such as photocatalyst, semiconductors, solar cells and pharmaceuticals. Many methods for synthesis of zinc oxide nanostructures have been reported in wet chemistry such as thermal decomposition, sol–gel techniques and precipitation [12].

Most preferably the adsorbent material choice is taken based on the easy availability, more adsorption, cost effective one. The present study focussed on the cost effective synthesis and application of nanomaterial for the treatment of carcinogenic dyes. Unexpectedly the property of synthesized zinc oxide nanostructures explores its application to the pharmaceutics against anticancer activities (antiproliferative efficacy against human melanoma).
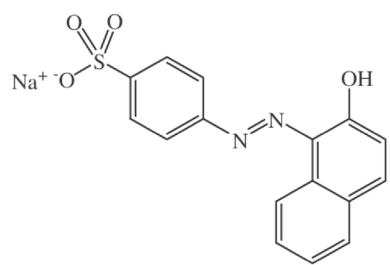
2 Materials and Methods

2.1 Materials

The chemicals used in this present research work such as zinc nitrate ($Zn(NO_3)_2$), sodium hydroxide (NaOH) and ethanol were of analytical grade with 99% purity, purchased from Sigma-Aldrich. Commercially available Acid orange 7 (AO7) dye was used without further purification (Table 2). 0.1 M NaOH and 0.1 M HCl were used to adjust the desired initial pH values of reaction mixtures.

2.2 Synthesis

The nanomaterial was synthesized by taking exactly 100 mL of 0.3 mol $Zn(NO_3)_2$ in a double-necked round bottom flask

Table 2 Colour index of Acid Orange 7 dye

Colour index	AO7
Name of the dye	Acid orange 7 (AO7)
Chemical formula	$C_{16}H_{11}N_2NaO_4S$
Structure of the dye	
Molecular mass (g/mol)	350.33
CAS registry number	633–96-5
λ_{max}	483 nm

and stirred continuously using a magnetic stirrer (REMI) at 100 rpm. To the reaction mixture 0.4 mol NaOH (S1) was added within a time span of 20 min under constant stirring. Then, the reaction mixture was heated in an oil bath for 5 h at 90 °C with constant stirring. After heating, the reaction mixture was allowed to cool naturally at room temperature. The white precipitate formed was separated by centrifuge at 5000 rpm for 10 min. The precipitate was washed thoroughly with double-distilled water and then washed several times with pure ethanol. Then, the precipitate was dried at 80 °C for 12 h in a hot-air oven. Finally, the precipitate was calcined at 550 °C for 1 h in a muffle furnace.

Similarly, the synthesis was performed with varying the concentrations of NaOH viz., 0.8, 1.0, 1.2 and 1.4 mol and the product obtained were named as S2, S3, S4 and S5, respectively. Finally, the products obtained were stored in airtight containers until further use.

2.3 Characterization

A Shimadzu XRD-6000 powder X-ray diffractometer was used to record the X-ray diffraction (XRD) patterns of the samples. Ni-filtered Cu Kα radiation was used at a tube voltage of 40 kV with tube current of 200 mA. Raman spectra measurements were made with a Bruker RFS 27 multi-RAM stand-alone FT-Raman spectrometer under the spectral range 4000 to 50 cm^{-1} at a resolution of 2 cm^{-1}. The source used was a 1064 nm Nd-YAG laser. Field emission scanning electron micrographs of the samples were obtained with a FEI Quanta FEG 200 scanning electron microscope (SEM). The energy dispersive X-ray (EDX) spectra were recorded using a FEI Quanta FEG 200 SEM with EDX attachment. The diffuse reflectance spectra of the samples were recorded with a PerkinElmer Lambda 950 UV/Vis/NIR spectrometer in the wavelength 175 to 3300 cm^{-1}. Surface area and porosity of the sample was scrutinized by nitrogen adsorption/desorption analysis (BET) using a Micrometrics ASAP 2020 apparatus at a relative pressure (P/P$_0$) range of 0.04–0.9.

2.4 Batch Adsorption Studies

The performance of synthesized sorbent materials (S1, S2, S3, S4 and S5) were analysed by batch experimental studies. A total of 100 mg of adsorbent dose was mixed with 100 mL of AO7 solution at different initial concentrations viz., 25, 50, 75 and 100 ppm at different temperature ranging from 30, 35, 40 and 45 °C. The pH of the reaction mixture was adjusted from 2, 4, 6, 8, 10, 11 and 12 by 0.1 M hydrochloric acid and 0.1 M sodium hydroxide. The reaction mixtures were agitated using a temperature-controlled Remi-make orbital shaker. The concentration of the residual dye in the clear supernatant solution at different time intervals from 0 to 100 min was estimated by measuring the absorbance using an Elico-make BL130- UV–Vis spectrometer. The dye degradation efficiency was estimated at the λ$_{max}$ value of 483 nm at different time intervals. All the adsorption experiments were performed in duplicate, and the maximum deviation allowed between the experiments was only 4%. The percentage of decolourization of dye was calculated as,

$$\text{Colour removal}(\%) = \left(\frac{C_0 - C_t}{C_0} \right) x 100 \tag{1}$$

where C_0 is the initial concentration of the dye solution and C_t is the concentration of the dye after the time interval t.

2.5 Antiproliferative Studies

The human melanoma cancer cell line (A-375) was procured from the National Centre for Cell Sciences (NCCS), India.

The cancer cells were allowed to grow in Dulbecco's modified Eagle medium (DMEM) with 2 mM of L-glutamine, and the cells were maintained with a balanced salt solution (BSS) that consisted of 1.5 g L^{-1} Na$_2$CO$_3$, 0.1 mM nonessential amino acids, 1 mM sodium pyruvate, 2 mM L-glutamine, 1.5 g L^{-1} glucose, 10 mM (4-(2-hydroxyethyl)-1-piperazine ethane sulfonic acid) (HEPES) and 10% fetal bovine serum (FBS) (Gibco, USA). Additionally, the cell was maintained at 37 °C with 5% CO$_2$ in a humidified CO$_2$ atmosphere. The pictorial representation is shown in Fig. 1.

The cytotoxic effect of the synthesized compound (IC$_{50}$) was tested by using MTT (3-(4,5-dimethylthiazol-2-yl)-2,5-diphenyltetrazolium bromide) assay. The cancer cell line (A-375) was allowed to grow (1 × 10^4 cells/well) in a 96-well plate for 48 h in order to obtain a confluence of 80%. It was followed by the replacement of the culture medium with a fresh medium containing various concentrations of synthesized compounds, and the cells were incubated for a further 48 h. The culture medium was removed and 100 µL of the MTT solution was added to each of the plates and incubated at 37 °C for 4 h. After removal of the supernatant, 10-min incubation was carried out adding 50 µL of DMSO to every well. The formazan crystals were dissolved. The optical density was measured at 620 nm in an ELISA multi-well plate reader (Thermo Multiskan EX, USA). The optical density (OD) value was used for estimating the percentage of viability using formula (2).

$$\% \text{ of viability} = \frac{\text{OD value of experimental sample}}{\text{OD value of experimental control}} \times 100 \tag{2}$$

The selected human melanoma cancer cells (A-375) were allowed to grow on cover-slips (1 × 10^5 cells/cover slip), and the cells were incubated with the synthesized ZnO nanostructures at different concentrations and fixed in ethanol–acetic acid solution (3:1, v/v). The cover slips were gently mounted on glass slides for morphometric analysis. Three monolayers were micrographed in each experimental group. The morphological alterations of the cells were analyzed using a Nikon (Japan) bright-field inverted light microscopy at 40 × magnification.
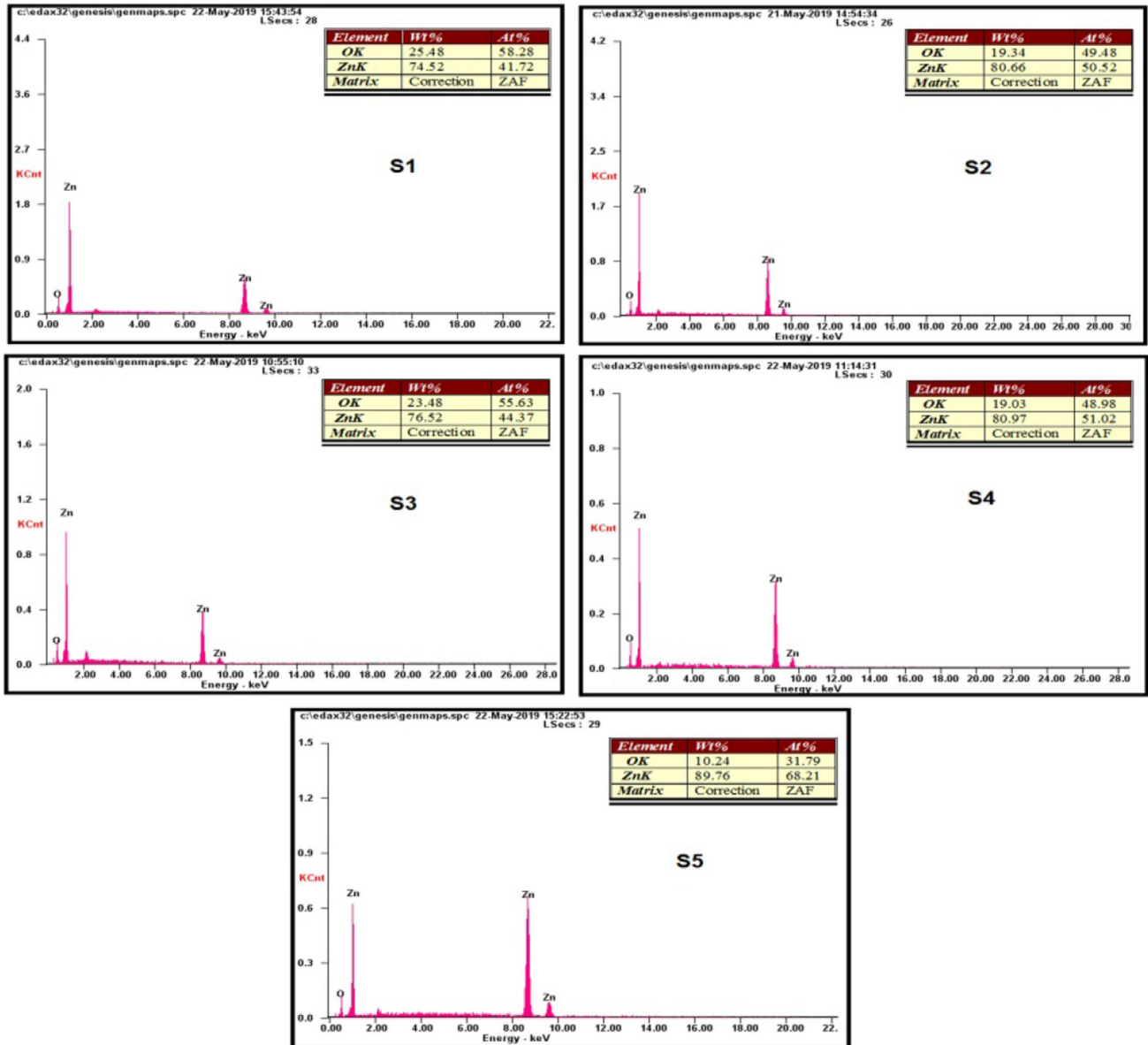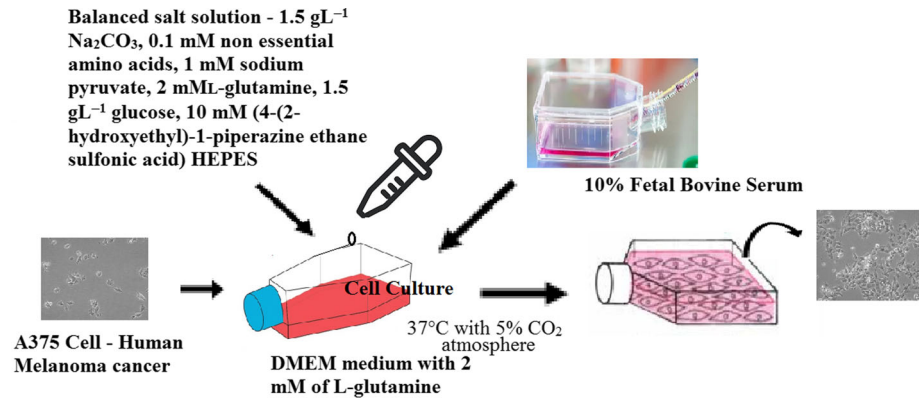
3 Results and Discussion
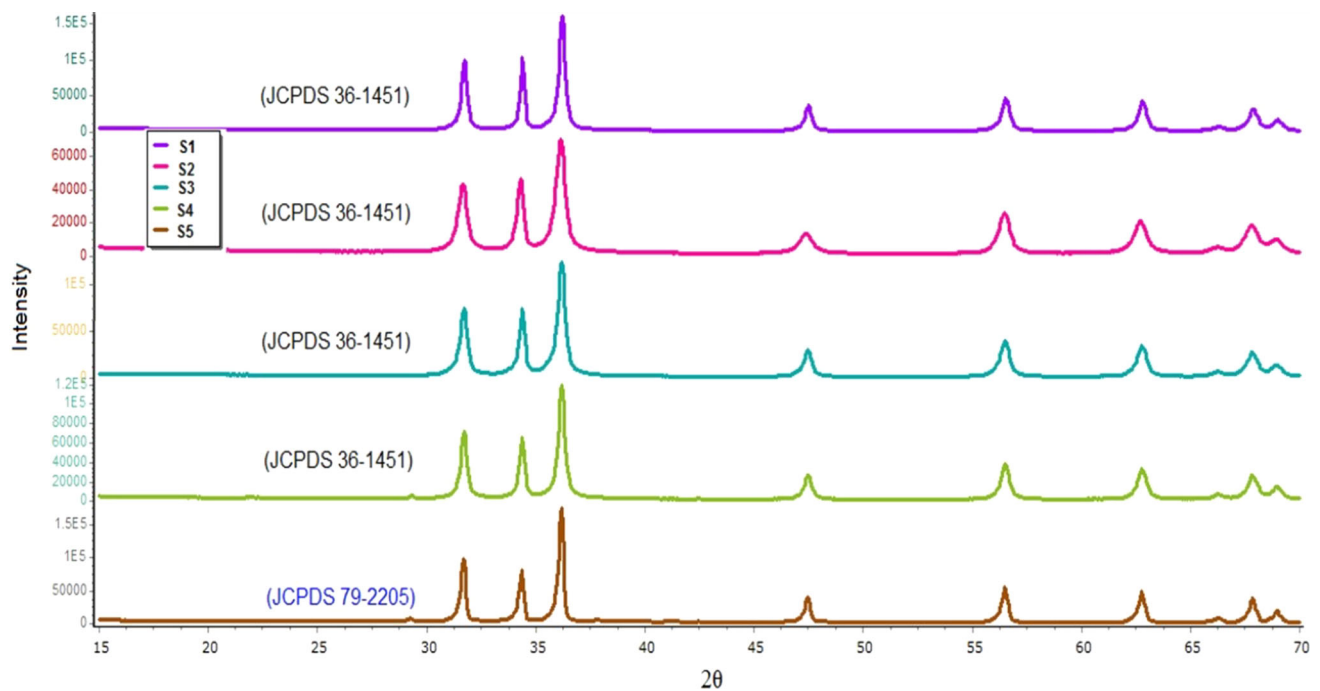
3.1 Characterization of ZnO Nanostructures

Figure 2 presents the EDX spectra of samples S1, S2, S3, S4 and S5. They show the presence of only zinc and oxygen and indicate the purity of the samples.

The powder XRD patterns of samples S1, S2, S3, S4 and S5 (Fig. 3) uniformly display diffraction peaks at 31.72°,

Fig. 1 Pictorial representation of cell culture

Balanced salt solution - 1.5 gL^{-1} Na$_2$CO$_3$, 0.1 mM non essential amino acids, 1 mM sodium pyruvate, 2 mM L-glutamine, 1.5 gL^{-1} glucose, 10 mM (4-(2-hydroxyethyl)-1-piperazine ethane sulfonic acid) HEPES

10% Fetal Bovine Serum

A375 Cell - Human Melanoma cancer

Cell Culture

37°C with 5% CO$_2$ atmosphere

DMEM medium with 2 mM of L-glutamine

Fig. 2 EDX spectra of ZnO nanostructures S1, S2, S3, S4 and S5

Fig. 3 XRD Spectra of ZnO nanostructures S1, S2, S3, S4 and S5

34.39°, 36.24°, 47.46°, 56.49°, 62.77° and 67.84°. These reflections correspond to 1 0 0-, 0 0 2-, 1 0 1-, 1 0 2-, 1 1 0-, 1 0 3- and 1 1 2-planes of hexagonal wurtzite crystalline lattice and the peak intensities are in agreement with the JCPDS Card No. 36–1451 for S1, S2, S3 and S4 ZnO samples and JCPDS 79–2205 for S5 ZnO sample. All the ZnO nanocrystals show intense 101—diffraction peak indicating preferential crystallographic 101—orientation. In particular, the sample S5 displays highly intense 101- peak, which may be due to hollow hexagonal tube-like structure, as seen from FE-SEM (vide infra). The average crystallite sizes of S1, S2, S3, S4 and S5 deduced from the XRD data are 26, 17, 22, 25 and 33 nm, respectively.

Raman spectroscopic analysis using the shift in bulk phonon frequencies are useful to infer structural disorder, defects like oxygen deficiency and surface impurities and phonon capturing in ZnO nanostructures [13]. The E_2 (high) peak is the characteristic optical phonon frequency for the perfect wurtzite hexagonal phase of ZnO crystal and is observed at 437 cm^{-1} [14]. This peak fits to the space group C_{6v}^4(28). The Raman E_2 (high) frequencies of the five synthesized ZnO nanostructures, shown in Fig. 4, have been compared with the theoretical [15, 16] and experimental values of bulk ZnO. The results indicate the gradual increase of the lattice defects on moving from sample S1 to sample S5. The ZnO nanostructure S5 shows maximum defects theoretically as well as comparatively. The proposition is in agreement with a couple of recent reports on Fe -doped ZnO films [17]. The Raman spectra of ZnO nanostructures S4 and
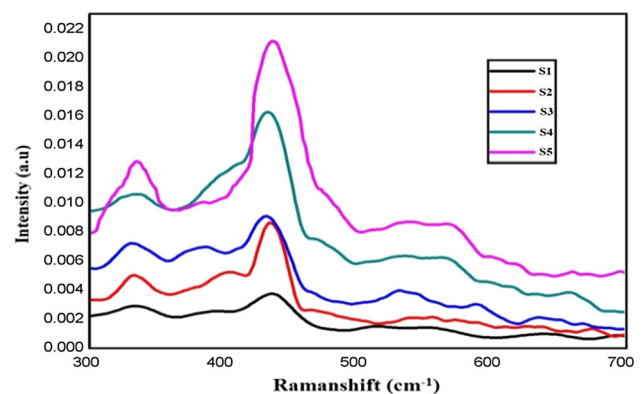

Fig. 4 Raman spectra of ZnO nanostructures S1, S2, S3, S4 and S5

S5 show the B1 peak at 297 cm^{-1} as broad and less intense, implies the existence of lattice defects in the nanostructures [18].

Sample S1 was prepared from 1:2 molar mixtures of precursors, and Fig. 5a shows morphology as a rectangular nanorod. The image suggests that rods are bundled prior to the separation. It is likely that the lowest concentration of sodium hydroxide enabled such formation. The length and width of the rods are nearly 400 nm and 30 nm, respectively. Figure 5b displays the plant leaves—like nanostructure (S2), which was obtained from 1:4 molar mixtures of the precursors. The large—scale plant leave—like structure is formed at the bottom of the collection. Most of the structures are uniform with length of upper leaves as less than 250 nm and

**Fig. 5** SEM images of ZnO nanostructures S1, S2, S3, S4 and S5
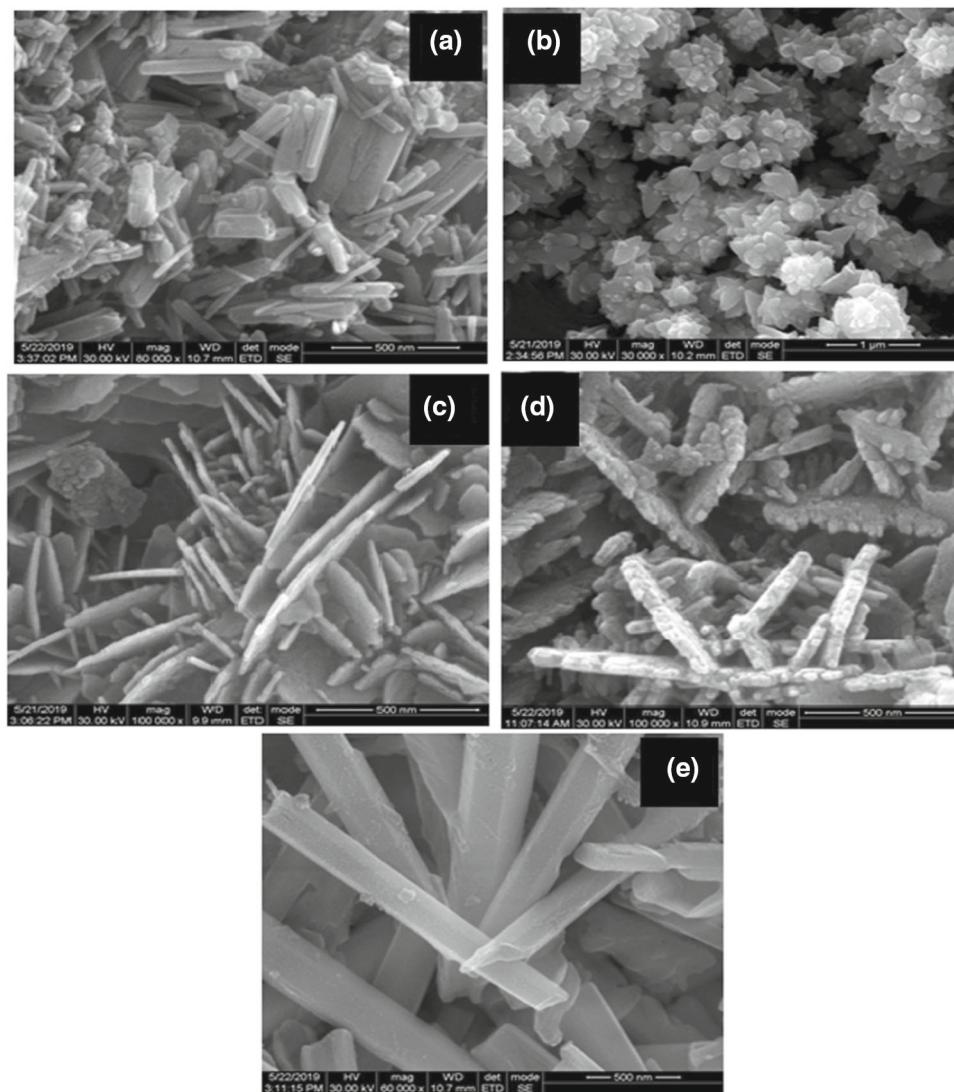
the length of bottom leaves more than 400 nm. All the leaves are tri-centred and look like the apex of the tri—leaf cannabis plant and the thickness of each leaf is about 30 to 40 nm.

Figure 5c depicts the morphology of the sample S3 synthesized with precursors at a molar ratio 1:6. The structure has many thin nanosheets joined collectively to form a single 3D flower—like aggregate. Figure 5d shows the SEM image of S4, obtained using the precursors in the molar ratio 1:8. The morphology of S4 imitates the morphology of S3, that is, 3D flower-like aggregate, and the nanosheets are of thickness ~ 30 nm. The SEM image of S5, the sample derived from the precursors at a molar ratio of 1:10, looks like hollow hexagonal nanotubes (HHNT), as displayed in Fig. 5e. The HHNT, compared to the other nanostructures S1, S2, S3 and S4, shows a good aspect ratio and exhibits a thickness of 20 to 30 nm. The crystal growth mechanism of HHNT is likely to be formation of nanosheet intermediates followed by rolling

over. However, the crystal growth mechanism of high–aspect–ratio hollow cylinders is not yet clear. Irrespective of the nano-ZnO morphology, all the synthesized samples (S1-S5) display the crystal pattern of hexagonal wurtzite ZnO.

The Kubelka–Munk (K-M) equation was used to calculate the band gap energies of the prepared samples from their reflectance spectra as shown in Fig. 6. Using the K-M equation, it is observed graphically that the band gap energies of S1, S2, S3, S4 and S5 are 3.189, 3.199, 3.222, 3.258 and 3.183 eV, respectively. The HHNT (S5) possesses the lowest band gap of 3.183 eV, with an absorption maximum of 397 nm in the UV region. Hence, S5 has been chosen for further studies.

Brunauer-Emmett-Teller (BET) gas sorption measurement was done to study the specific surface areas and the porous nature of the adsorbent ZnO nanostructure. It is evident from Fig. 7 that the nitrogen adsorption/desorption isotherm is in accordance with type IV isotherm given by
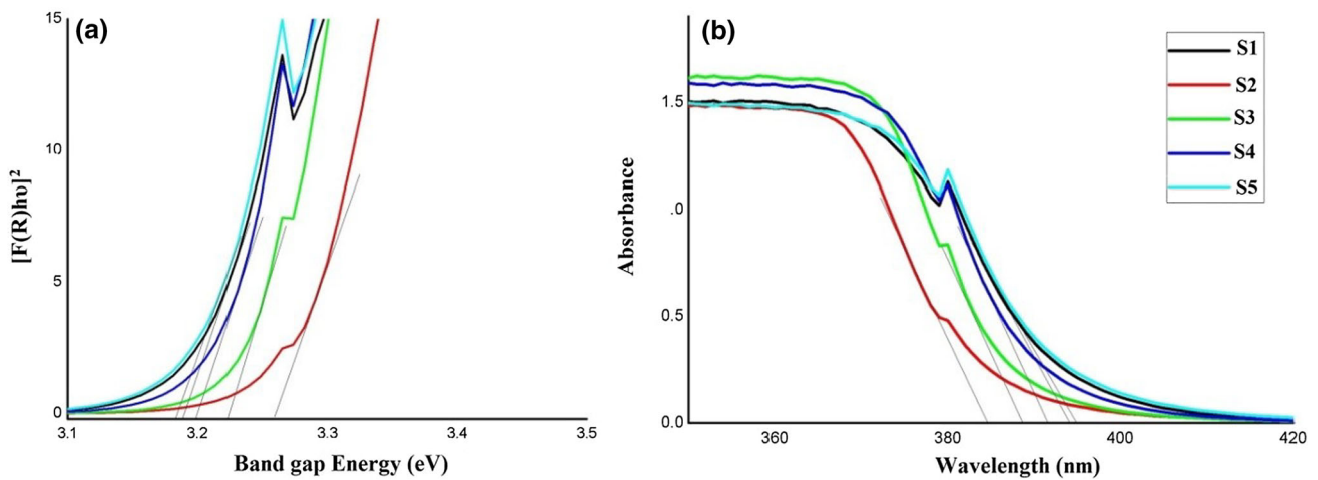
Fig. 6 Graphical representation of modified Kubelka–Munk: $[F(R)h\upsilon]2$ Vs. **a** band gap energy and **b** corresponding absorption spectra of the ZnO samples S1 to S5
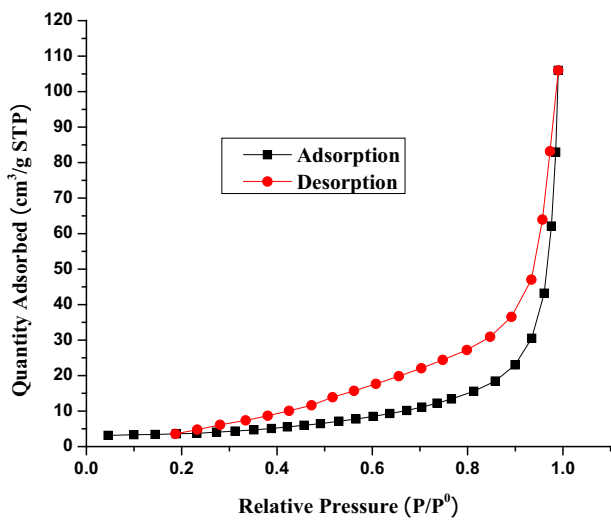
Fig. 7 Protonation of dye species at lower pH
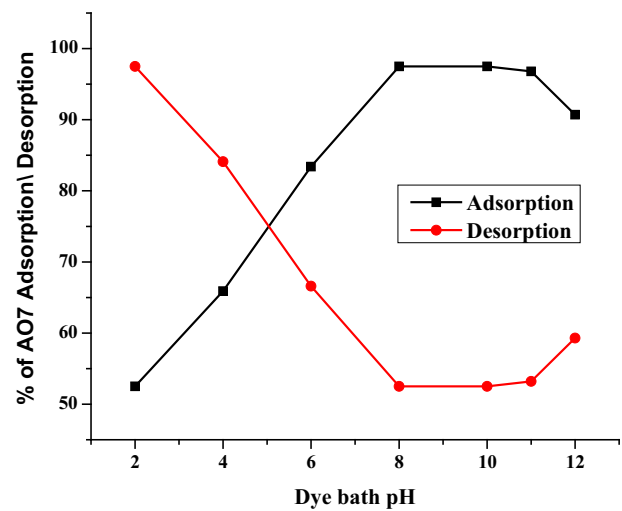
Fig. 8 Variation of AO7 adsorption/desorption with respect to the dye bath pH

IUPAC classification and the mesoporous nature of the ZnO nanostructure was confirmed from the P/P_0 graph, where the adsorption/desorption curve increases from 0.6–1.0 and the pore diameter is approximately 50 nm. Similar results were explained by Shamhari et al. [19], Ismail et al. [20]. Mesoporous nature and the larger pore size of the ZnO nanostructures support the easy diffusion of dye molecule and hence can be used as a good adsorbent for wastewater treatment.

3.2 Adsorption Studies

3.2.1 Effect of pH on Adsorption and Desorption

The pH of the adsorbate solution is one of the influential parameters in adsorption studies, and hence, the experiments

are carried out at different initial of pH from 2, 4, 6, 8, 10, 11 and 12. The adsorption of contaminant on ZnO nanostructures is susceptible to the surface charge of the adsorbent and speciation of the contaminant in solution, both of which are influenced by the initial pH of the adsorbate solution [21, 22]. This results in electrostatic attraction/repulsion among the sorbent and solute interface. The pK_a value of AO7 ($pK_a = 8.26$) indicates that the extent of ionization of dye molecules is very low. Although the dye ionizes feasibly, shows better adsorption in a neutral/basic solution (pH > 7).

Figure 8 shows the variation of AO7 adsorption with respect to the dye bath pH. The point of zero charge (pH_{zpc}) suggests the pH value required for the sorbent surface to possess a neutral charge. The pH_{zpc} of ZnO nanostructures are about 10.1 ± 0.6. The anionic dye species $[AO7]^-$ shows an
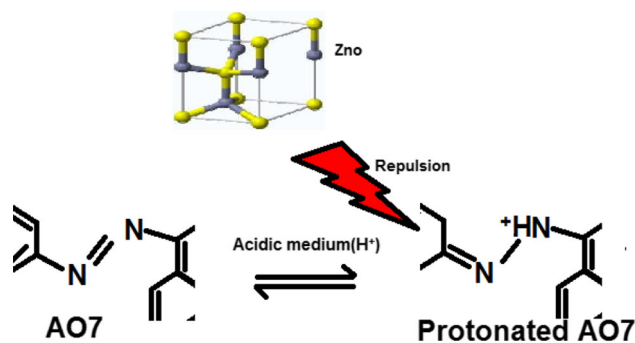
Fig. 9 Pictorial representation of AO7 adsorption at lower pH

increase of adsorption with increasing pH from 2.0 to 8.0. The maximum AO7 dye adsorption of 97.5% over the adsorbent ZnO nanostructure is found to be at pH 8. On increasing the pH above pH$_{zpc}$ of ZnO, the sorbent surface acquires a negative charge and reveals electrostatic repulsion of the dye molecule because of the anionic nature of the dye and decrease of dye adsorption on ZnO [23]. Figure 9 depicts the pictorial representation of AO7 adsorption at lower pH. At lower pH, the protons may attach with any of the nitrogen present in the azo double bond of the dye and hence gets protonated. Thus, a repulsive force is generated between protonated AO7 dye with anionic ZnO nanostructures resulted in decrease in adsorption of dye species. In addition, the part dissolution of ZnO nanostructures in acidic solutions decreases the number of active sites of ZnO nanostructures. Similar observations were reported in the literature for other acidic dyes [24, 25].

Desorption studies of AO7 loaded on ZnO nanostructures are conducted to identify the nature of interaction between the sorbent and the sorbate molecules. AO7-loaded ZnO is shaken well with distilled water by varying its pH from 2 to 12 (Fig. 8). At lower pH, maximum amount of AO7 is eluted. Hence, acidic water with lower value of pH is identified as the suitable eluent for regenerating spent ZnO and substantiates the weak interaction of AO7 on ZnO surface. As acidic medium may hamper the ZnO nanostructure, 5% NaOH solution and ethanol are used to estimate the recyclability. The regeneration efficiency is found to be good and reaches about 80% up to 5 cycles, after which it decreases with every successive cycle.

3.2.2 Effect of Temperature

Temperature is another important factor for adsorption, and the equilibrium was studied by adsorption thermodynamics by varying the temperature from 30° to 45 °C. Figure 10 depicts the adsorption capacity of ZnO (100 mg) for AO7 dye at the initial concentration of 50 mg L^{-1} as a function of temperature from 30° to 45 °C and it clearly substantiates that an increase in the temperature of the dye bath decreases the adsorption of AO7 dye from 48.68 mg g^{-1} to 43.34 mg g^{-1}. This implies that nature of the sorption process is exothermic. A possible reason is that an increase in temperature decreases the adsorptive force among AO7 species and active sites on the ZnO surface [26].

3.2.3 Adsorption Kinetics

The adsorption kinetics is analyzed using the experimental data by employing common kinetic models, namely

Fig. 10 Effect of temperature on adsorption of AO7 dye
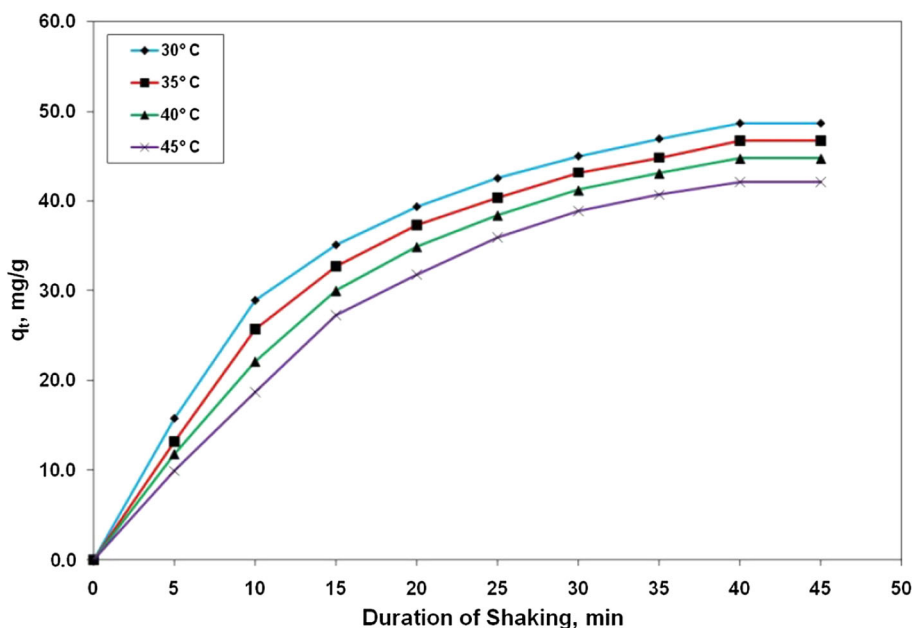
Table 3 Pseudo-first-order and second-order kinetic parameters for AO7-adsorption on nano-ZnO

Parameters	Dye bath Temperature °C								Initial dye concentration, mg/L							
	Linear				Nonlinear				Linear				Nonlinear			
	30	35	40	45	30	35	40	45	25	50	75	100	25	50	75	100
$q_e$exp.(mg/g)	48.60	47.04	45.53	43.34	48.60	47.04	45.53	43.34	25.00	48.68	70.98	90.67	25.00	48.68	70.98	90.67
Pseudo-first-order kinetics																
k_1 (min -1)	0.0912	0.0944	0.0958	0.0972	0.0803	0.0710	0.0623	0.0546	0.0762	0.0921	0.0995	0.1023	0.1069	0.0803	0.0711	0.0654
$q_e$cal(mg/g)	52.00	54.85	56.10	56.00	49.95	49.05	48.46	47.41	18.52	52.29	90.16	129.06	24.84	49.95	74.14	96.67
r^2	0.9894	0.9887	0.9840	0.9778	0.9983	0.9983	0.9987	0.9966	0.9488	0.9884	0.9696	0.9569	0.9972	0.9983	0.9988	0.9994
Sd	1.200	2.761	3.739	4.478	0.475	0.709	1.037	1.439	2.290	1.274	6.779	13.575	0.057	0.447	1.117	2.124
Pseudo-second-order kinetics																
k_2(g/mg/min)	0.0024	0.0019	0.0017	0.0014	0.0012	0.0010	0.0008	0.0007	0.0024	0.0019	0.0017	0.0014	0.0012	0.0010	0.0008	0.0007
$q_e$cal(mg/g)	56.18	55.87	55.25	54.64	64.12	64.81	65.94	66.65	56.18	55.87	55.25	54.64	64.12	64.81	65.94	66.65
r^2	0.9562	0.9340	0.9116	0.8710	0.9968	0.9951	0.9951	0.9924	0.9562	0.9340	0.9116	0.8710	0.9968	0.9951	0.9951	0.9924
Sd	2.678	3.119	3.436	3.998	5.485	6.282	7.215	8.242	2.678	3.119	3.436	3.998	5.485	6.282	7.215	8.242

Table 4 Parameters of AO7 adsorption Isotherm

Parameters	AO7 dye							
	Linear model				Nonlinear model			
	Dye bath temperature °C							
	30	35	40	45	30	35	40	45
Langmuir isotherm								
Q_0 (mg/g)	90.91	86.21	88.50	90.91	98.98	92.92	86.94	91.95
b_L (L/mg)	0.0107	0.0113	0.0126	0.0198	0.2665	0.2407	0.1779	0.0877
r^2	0.9605	0.9655	0.9836	0.9865	0.9786	0.9788	0.9758	0.9866
Sd	–	–	–	–	3.84	3.61	3.57	2.46
Freundlich isotherm								
n	1.841	1.953	2.066	1.783	2.811	2.746	2.435	2.069
k_f(mg/g).(L/g)$^{1/n}$	19.512	18.378	16.315	10.617	9334.9	12,162	1386.7	205.74
r^2	0.8444	0.8635	0.9629	0.9695	0.9879	0.9861	0.9825	0.9897
Sd	–	–	–	–	2.89	2.92	3.03	2.16

Langergren pseudo-first-order and Ho and McKay pseudo-second-order kinetic models. These kinetic data provide useful information about the sorption pathways and their related mechanism [27–29]. From the experimental data, the values q_e and k_1 are calculated by plotting q_t vs. t for nonlinear and $\log(q_e - q_t)$ vs. t for linear expression for the pseudo-first-order kinetic model. Similarly, for pseudo-second-order, q_e and k_2 are calculated by nonlinear curve fitting with t/q_t vs. t and linear fitting with q_t vs. t.

The calculated kinetic results of linear and nonlinear models are tabulated in Table 3 with respect to the initial concentration of AO7 dye (from 25 to 100 mg/L) and dye bath temperature (from 30° to 45 °C). It is inferred that, while increasing initial dye concentration from 25 to 100 mg/L, the pseudo-first-order rate constant increased from 0.0762 to 0.1023 min^{-1} for the linear model and decreased from 0.1069 to 0.0654 min^{-1} for the nonlinear model, respectively. Similarly, under different temperatures, k_1 value increases from 0.0912 to 0.0972 min^{-1} for the linear model, and for nonlinear model, it decreases from 0.0803 to 0.0546 min^{-1}. Thus, it is clearly seen that the nonlinear model shows a coherent variation, whereas no sequential variation of rate constant is found in the linear model with respect to concentration and temperature of the dye bath.

It is observed that the nonlinear form of pseudo-first-order and pseudo-second-order fits represent the experimental data in a better way when compared with linear forms. The q_e(exp) values always increase as a function of initial concentration of dye (from 25.00 to 90.67 mg/g), and the q_e(cal) values (from 24.84 to 96.67 mg/g) also follow the same trend as Shukla et al. [30].

Furthermore, the q_e(cal) values of the pseudo-first-order kinetic model harmonize with the q_e(exp) values than in the

case of the pseudo-second-order kinetic model. In addition, the values of the correlation coefficient r^2 for pseudo-first-order kinetics are relatively higher than the pseudo-second-order kinetics. Hence, from kinetic analysis, it is concluded that the best fit kinetic model to explain the adsorption of AO7 dye onto ZnO surface is the nonlinear form of pseudo-first-order model [31].

3.2.4 Adsorption Isotherm

The isotherm model provides knowledge about the affinity between the adsorbate and adsorbent, which enables us to predict the nature and mechanism of interaction [32]. In this study, the equilibrium data of AO7 adsorption on ZnO were analyzed by employing the isotherms of Langmuir and Freundlich.

Table 4 represents the isotherm parameters for the removal of AO7 dye by ZnO adsorbent. For the linear model, the value of Langmuir constant (b_L) increases from 0.0107 to 0.0198 (L mg^{-1}) as the dye bath temperature is raised from 30 °C to 45 °C, and for the nonlinear model, the b_L constant decreases from 0.2665 to 0.0877 L mg^{-1} for the same temperature range. In the case of the nonlinear model, the exothermic nature of the adsorption process is supported by the decrease in b_L value with increase in temperature from 30 °C to 45 °C. Out of the two models, the Freundlich model (0.9825–0.9897) is slightly better in respect of r^2 as compared to the Langmuir isotherm (0.9786–0.9866). The nonlinear data exhibit the best fit with high r^2 value than the linear data. The sorption process is favorable if the value of "n" lies in the Freundlich threshold range, that is, $n = 1$ to 10 [33]. Hence, it is proposed that the adsorption process of
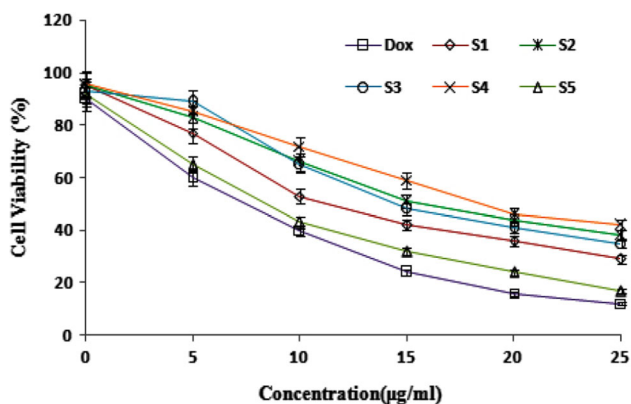
Fig. 11 Cytotoxic efficacy of synthesized ZnO nanostructures against human melanoma cancer cells

the present study is multilayered and occurs on the heterogeneous surface of the sorbent material.

3.2.5 Adsorption thermodynamics

For validating the nature of adsorption of AO7 onto the ZnO surface, the thermodynamic parameters such as free energy (ΔG) and enthalpy (ΔH) are estimated. In this study, Langmuir constant b_L (L mg^{-1}) is modified to k_L (mol L^{-1}) by involving the molecular weight of AO7 [34] and Eq. 3 is employed to evaluate the free energy.

$$\Delta G = -RT \ln k_L \qquad (3)$$

where the gas constant, $R = 8.314$ J K^{-1} mol^{-1}, T is the temperature of dye bath in Kelvin and k_L is the Langmuir adsorption equilibrium constant (mol L^{-1}). The value of k_L indicates the affinity between the adsorbent and the adsorbate. The negative value of ΔH, -31.06 kJ/mol signifies physical adsorption and exothermic in nature. Furthermore, the negative ΔG values -3.44, -3.625, -3.977 and -5.235 kJ/mol with respect to the temperature from 30, 35, 40 and 45 °C, respectively, suggest the spontaneity of the adsorption process. Value of ΔS -113.16 J/Kmol shows less randomness of the adsorption process because of association of AO7 on ZnO nanostructure [34].

3.3 Antiproliferative Efficacy Against Melanoma Cancer Cells

3.3.1 Cytotoxic Assay

The influence of the synthesized nanostructured ZnO on human melanoma cancer cells has been studied using MTT assay. Figure 11 indicates the in vitro cytotoxic effect of the synthesized ZnO (0–25 µg mL^{-1}) on the selected A-375 melanoma cancer cells. The experimental results validate that all the synthesized nanomaterials dose-dependently inhibit the proliferation of the cancer cells in a significant manner. Sample S5 shows a higher efficacy in controlling the proliferation of the human melanoma cancer cells, with the lowest IC$_{50}$ concentration (8 µg mL^{-1}), when compared with the other samples. Though S5 (obtained with 1:10 precursors) exhibits a significant anticancer potency, it is not able to reach the effectiveness of the conventional drug doxorubicin. A previous study reveals that the synthesized ZnO nanorods are able to exhibit cytotoxicity of about 22 and 20 µg mL^{-1} against liver cancer cells for 24 h and 48 h, respectively [35]. Another study stated that the ZnO nanoparticles show an IC$_{50}$ concentration of 10 µg mL^{-1} against the MCF-7 breast cancer cells [36]. An additional report depicts that the inhibitory concentration of DOX-ZnO nanoparticles is 0.125 µg mL^{-1} for MCF-7 and HT-29 cells [37].

3.3.2 Analysis of Morphological Alteration Upon Treatment

After MTT analysis of the five synthesized nanostructured ZnO, S5 (1:10) shows a significant cytotoxic inhibitory activity and is further evaluated for cancer cell morphological alteration potential. The alterations occur in the cancer cell morphology upon treatment with the synthesized ZnO at different concentration, as shown in Fig. 12. The control cells do not show any noticeable changes in their morphology, whereas the nanostructured ZnO-treated cells display appreciable changes on treatment including cell shrinkage, membrane blebbing and formation of floating cells.

These alterations occur based on the concentration in which the cells have been treated. Thus, the antiproliferative effect of the synthesized nanostructures may be linked with its ability to disrupt the morphology of the cells. According to a previous study Ashokan et al. [35], the treated cells exhibit severe morphological changes including formless shape, detached and floating from the cell surface at higher concentrations. Zinc oxide nanoparticles induce apoptosis in melanoma cells by increasing ROS and this effect may be mediated by the ROS-dependent induction of p53 in treated cells [38]. This clearly demonstrates the central role of ZnO materials in ZnO-induced apoptosis of cancer cells. Further studies are warranted to ascertain the potential usefulness of zinc oxide nanorods to correcting the dysregulation of apoptosis in the therapy of melanoma.

4 Conclusion

Different morphological ZnO nanomaterials have been successfully synthesized by sol–gel method. Characterisation of synthesized material using SEM, EDAX, XRD, BET and Raman spectra ensures the nanostructure crystal pattern of
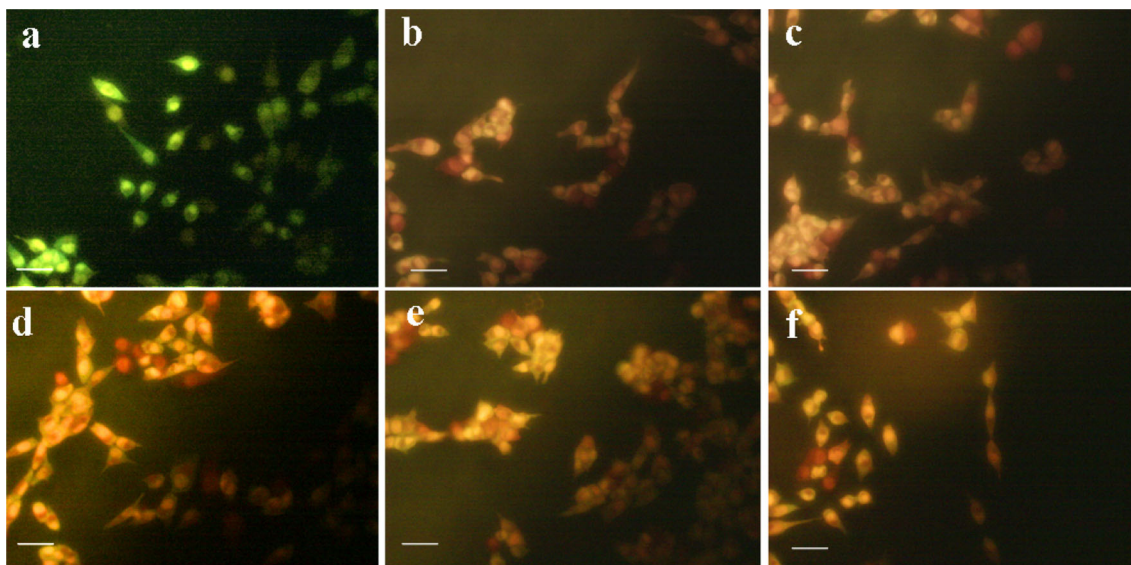
Fig. 12 Apoptotic analysis of synthesized zinc nanostructures using A375 cells with AO/EtBr **a** Control **b-f** samples. Scale bar- 50 μm

hexagonal wurtzite ZnO. Based on the characterization studies sample S5 has been chosen for the decolourisation of AO7 dye by adsorption method. From the kinetic analysis data, confirm the adsorption of AO7 dye onto ZnO surface is nonlinear form of pseudo-first-order model. Isotherm studies showed that Freundlich isotherm explains the adsorption process more clearly than Langmuir adsorption isotherm. The thermodynamic analysis reveals that the process is spontaneous, exothermic and less randomness. Furthermore, the identified nano-ZnO extends its application towards the pharmaceutical application. S5 (nanorod) exhibits increased anti-melanoma cancer efficacy when compared with the other synthesized nanostructures. Thus, the synthesized nanorod is found to have anticancer properties and is also an efficient adsorbent of hazardous dyes from aqueous dye solution.

References

1. Zhou, Y.; Lu, J.; Zhou, Y.; Liu, Y.: Recent advances for dyes removal using novel adsorbents: A review. Environ Pollut. (2019). https://doi.org/10.1016/j.envpol.2019.05.072
2. Sakthisharmila, P.; Palanisamy, P.N.; Manikandan, P.: Removal of benzidine based textile dye using different metal hydroxides generated in situ electrochemical treatment-A comparative study. J. Clean. Prod. (2018). https://doi.org/10.1016/j.jclepro.2017.11.192
3. Manjula Rani, K.; Palanisamy, P.N.: Kinetics and isotherm studies for the adsorptive removal of Reactive Red-141 dye from aqueous solution by uncalcined and calcined zinc aluminium carbonate layered double hydroxide- A comparative study. Indian J. Chem. Technol. **25**(2), 179–188 (2018)
4. Abebe, B.; Ananda Murthy, H.C.; Dessie, Y.: Synthesis and characterization of Ti–Fe oxide nanomaterials: adsorption-degradation of methyl orange dye. Arab. J. Sci. Eng. (2020). https://doi.org/10.1007/s13369-019-04328-1
5. Naraghi, B.; Zabihi, F.; Narooie, M.R.; Saeidi, M.; Biglari, H.: Removal of Acid Orange 7 dye from aqueous solutions by adsorption onto Kenya tea pulps granulated shape. Electr. Phys. (2017). https://doi.org/10.19082/4312
6. Khosla, E.; Kaur, S.; Dave, P.N.: Mechanistic study of adsorption of acid orange-7 over Aluminum oxide nanoparticles. J. Eng. (2013). https://doi.org/10.1155/2013/593534
7. Sillanpää, M.; Mahvi, A.H.; Balarak, D.; Khatibi, A.D.: Adsorption of Acid orange 7 dyes from aqueous solution using Polypyrrole/nanosilica composite: Experimental and modelling. Int. J. Environ. Anal. Chem. (2021). https://doi.org/10.1080/03067319.2020.1855338
8. Wang, M.; Liu, X.; Pan, B.; Zhang, S.: Photodegradation of Acid Orange 7 in a UV/acetylacetone process. Chemosphere (2013). https://doi.org/10.1016/j.chemosphere.2013.08.082
9. Fernandes, A.: Electrochemical degradation of C I Acid Orange 7. Dyes Pigm. (2004). https://doi.org/10.1016/j.dyepig.2003.11.008
10. Rasmussen, J.W.; Martinez, E.; Louka, P.; Wingett, D.G.: Zinc oxide nanoparticles for selective destruction of tumor cells and potential for drug delivery applications. Expert Opin. Drug Deliv. (2010). https://doi.org/10.1517/17425247.2010.502560
11. Vaseem, M.; Umar, A.; Hahn, Y.-B.: ZnO Nanoparticles: Growth, Properties, and Applications. In: Umar, A.; Hahn, Y.-B. (Eds.) 5, pp. 1–36. American Scientific Publishers, California (2010)
12. Mahamuni, P.P.; Patil, P.M.; Dhanavade, M.J.; Badiger, M.V.; Shadija, P.G.; Lokhande, A.C.; Bohara, R.A.: Synthesis and characterization of zinc oxide nanoparticles by using polyol chemistry for their antimicrobial and antibiofilm activity. Biochem. Biophys. Rep. (2019). https://doi.org/10.1016/j.bbrep.2018.11.007
13. Giri, P.K.; Bhattacharyya, S.; Singh, D.K.; Kesavamoorthy, R.; Panigrahi, B.K.; Nair, K.G.M.: Correlation between microstructure and optical properties of ZnO nanoparticles synthesized by ball milling. J. Appl. Phys. (2007). https://doi.org/10.1063/1.2804012

14. Fonoberov, V.A.; Balandin, A.A.: ZnO quantum dots: physical properties and optoelectronic applications. J. Nanoelectron. Optoelectron. (2006). https://doi.org/10.1166/jno.2006.002

15. Richardson, H.H.; Hickman, Z.N.; Govorov, A.O.; Thomas, A.C.; Zhang, W.; Kordesch, M.E.: Thermooptical properties of gold nanoparticles embedded in ice: characterization of heat generation and melting. Nano Lett. **6**(4), 783–788 (2006)

16. Khan, A.; Kordesch, M.E.: Synthesis of novel zinc oxide microphone-like microstructures. Mater. Lett. (2008). https://doi.org/10.1016/j.matlet.2007.05.005

17. Srinivasulu, T.; Saritha, K.; Reddy, K.T.R.: Synthesis and characterization of Fe-doped ZnO thin films deposited by chemical spray pyrolysis. Modern Electr. Mater. (2017). https://doi.org/10.1016/j.moem.2017.07.001

18. Manjón, F.J.; Marí, B.; Serrano, J.; Romero, A.H.: Silent Raman modes in zinc oxide and related nitrides. J. Appl. Phys. (2005). https://doi.org/10.1063/1.1856222

19. Shamhari, N.M.; Wee, B.S.; Chin, S.F.; Kok, K.Y.: Synthesis and characterization of zinc oxide nanoparticles with small particle size distribution. Acta Chim. Slov. (2018). https://doi.org/10.17344/acsi.2018.4213

20. Ismail, M.A.; Taha, K.K.; Modwi, A.; Khezami, L.: ZnO nanoparticles: surface and X-ray profile analysis. J. Ovonic Res. **14**, 381–393 (2018)

21. Khedri, A.; Jafari, D.; Esfandyari, M.: Adsorption of Nickel(II) ions from synthetic wastewater using activated carbon prepared from *MespilusGermanica* leaf. Arab. J. Sci. Eng. (2021). https://doi.org/10.1007/s13369-021-06014-7

22. Gayathri, K.; Palanisamy, N.: Methylene blue adsorption onto an eco-friendly modified polyacrylamide/graphite composites: Investigation of kinetics, equilibrium, and thermodynamic studies. Sep. Sci. Technol. (2019). https://doi.org/10.1080/01496395.2019.1577261

23. Prola, L.D.T.; Acayanka, E.; Lima, E.C.; Umpierres, C.S.; Vaghetti, J.C.P.; Santos, W.O.; Laminsi, S.; Djifon, P.T.: Comparison of Jatropha curcas shells in natural form and treated by non-thermal plasma as biosorbents for removal of Reactive Red 120 textile dye from aqueous solution. Ind. Crops Prod. (2013). https://doi.org/10.1016/j.indcrop.2013.02.018

24. Bian, S.-W.; Mudunkotuwa, I.A.; Rupasinghe, T.; Grassian, V.H.: Aggregation and dissolution of 4 nm ZnO nanoparticles in aqueous environments: influence of pH, ionic strength, size, and adsorption of humic acid. Langmuir (2011). https://doi.org/10.1021/la200570n

25. Zafar, M.N.; Dar, Q.; Nawaz, F.; Zafar, M.N.; Iqbal, M.; Nazar, M.F.: Effective adsorptive removal of azo dyes over spherical ZnO nanoparticles. J. Market. Res. (2019). https://doi.org/10.1016/j.jmrt.2018.06.002

26. Zhang, F.; Lan, J.; Yang, Y.; Wei, T.; Tan, R.; Song, W.: Adsorption behavior and mechanism of methyl blue on zinc oxide nanoparticles. J. Nanopart. Res. (2013). https://doi.org/10.1007/s11051-013-2034-2

27. Yagub, M.T.; Sen, T.K.; Afroze, S.; Ang, H.M.: Dye and its removal from aqueous solution by adsorption: a review. Adv. Colloid Interf. Sci. (2014). https://doi.org/10.1016/j.cis.2014.04.002

28. Gupt, C.B.; Bordoloi, S.; Sekharan, S.; Sarmah, A.K.: Adsorption characteristics of Barmer bentonite for hazardous waste containment application. J. Hazard Mater. (2020). https://doi.org/10.1016/j.jhazmat.2020.122594

29. Ayawei, N.; Ebelegi, A.N.; Wankasi, D.: Modelling and interpretation of adsorption isotherms. J. Chem. (2017). https://doi.org/10.1155/2017/3039817

30. Shukla, S.P.; MarkandeyaKisku, G.C.: Linear and non-linear kinetic modeling for adsorption of disperse dye in batch process. Res. J. Environ. Toxicol. (2015). https://doi.org/10.3923/rjet.2015.320.331

31. de Farias Silva, C.E.; da Gama, B.M.V.; da Silva Gonçalves, A.H.; Medeiros, J.A.; de Souza Abud, A.K.: Basic-dye adsorption in albedo residue: Effect of pH, contact time, temperature, dye concentration, biomass dosage, rotation and ionic strength. J. King Saud Univ.-Eng. Sci. **32**(6), 351–359 (2020)

32. Chen, L.; Li, Y.; Du, Q.; Wang, Z.; Xia, Y.; Yedinak, E.; Lou, J.; Ci, L.: High performance agar/graphene oxide composite aerogel for methylene blue removal. Carbohydr. Polym. (2017). https://doi.org/10.1016/j.carbpol.2016.08.047

33. Ahmadi, S.; Mohammadi, L.; Rahdar, A.; Rahdar, S.; Dehghani, R.; Igwegbe, C.A.; Kyzas, G.Z.: Acid dye removal from aqueous solution by using Neodymium(III) Oxide Nanoadsorbents. Nanomaterials (Basel). (2020). https://doi.org/10.3390/nano10030556

34. Liu, Y.: Is the free energy change of adsorption correctly calculated? J. Chem. Eng. Data. **54**(7), 1981–1985 (2009)

35. Ashokan, A.P.; Paulpandi, M.; Dinesh, D.; Murugan, K.; Vadivalagan, C.; Benelli, G.: Toxicity on dengue mosquito vectors through myristica fragrans-synthesized zinc oxide nanorods, and their cytotoxic effects on liver cancer cells (HepG2). J. Cluster Sci. (2016). https://doi.org/10.1007/s10876-016-1075-y

36. Kavithaa, K.; Paulpandi, M.; Padma, P.R.; Sumathi, S.: Induction of intrinsic apoptotic pathway and cell cycle arrest via baicalein loaded iron oxide nanoparticles as a competent nano-mediated system for triple negative breast cancer therapy. RSC Adv. **6**, 64531–64543 (2016)

37. Vimala, K.; Sundarraj, S.; Paulpandi, M.; Vengatesan, S.: Green synthesized doxorubicin loaded zinc oxide nanoparticles regulates the Bax and Bcl-2 expression in breast and colon carcinoma. Process Biochem. **49**, 160–172 (2014)

38. Provinciali, M.; Pierpaoli, E.; Bartozzi, B.; Bernardini, G.: Zinc induces apoptosis of human melanoma cells, increasing reactive oxygen species, p53 and FAS ligand. Anticancer Res. **35**, 5309–5316 (2015)